ARTICLE

Open Access

Direct observation of the atomic density fluctuation originating from the first sharp diffraction peak in SiO$_2$ glass

Akihiko Hirata [1,2,3,4,5], Shuya Sato[6], Motoki Shiga [7,8,9], Yohei Onodera[5,10], Koji Kimoto [5] and Shinji Kohara [5,6]

Abstract
The intermediate-range order of covalently bonded glasses has been extensively studied in terms of their diffraction peaks observed at low scattering angles; these peaks are called the first sharp diffraction peaks (FSDPs). Although the atomic density fluctuations originating from the quasilattice planes are a critical scientific target, direct experimental observations of these fluctuations are still lacking. Here, we report the direct observation of the atomic density fluctuations in silica glass by energy-filtered angstrom-beam electron diffraction. The correspondence between the local electron diffraction patterns of FSDPs and the atomic configurations constructed based on the X-ray and neutron diffraction results revealed that the local atomic density fluctuations originated from the quasi-periodic alternating arrangements of the columnar chain-like atomic configurations and interstitial tubular voids, as in crystals. We also discovered longer-range fluctuations associated with the shoulder of the FSDP on the low-Q side. The hierarchical fluctuations inherent in materials could aid in the elucidation of their properties and performance.

Introduction

Understanding the intermediate-range order (IRO) in glasses beyond the nearest neighbor distances is one of the most intriguing topics in glass science[1–6]. For example, tetrahedral SiO$_4$ units in SiO$_2$ glass have been proposed to be interconnected to form several different-sized rings with corner-sharing motifs, which is typical of network glass[7]. These ring structures could be an aspect of the formation of IRO on the length scale[8–13]. Scattering experiments provide a distinct signature of the IRO through the diffraction peaks observed at low scattering angles in reciprocal space. Indeed, a diffraction peak called the first sharp diffraction peak (FSDP) can be observed in the structure factors of various covalent glasses ranging from $Q = 1$ to $2\,\text{Å}^{-1}$ [14–24]. The

characteristics and unusual properties of FSDPs have also been extensively reported[25–28]. Nevertheless, the IRO based on diffraction data is challenging to discuss due to the randomness and complexity of glass structures.

There are several interpretations of the origin of the FSDP. For example, Elliott proposed that FSDP originated from the chemical ordering of interstitial voids around the cation-centered clusters in a glass structure[15,16,23]. The ordering arising from the interstitial voids contributed to the formation of a pre-peak in the concentration–concentration partial structure factor. Another possible interpretation was provided by Gaskell and Wallis, as follows: the FSDP arises from the quasilattice planes in glass analogous to the Bragg planes in crystals[19]. They focused on the anisotropic scattering from local structure models and suggested that this scattering intensity was related to the periodic fluctuations in the atomic density. The fluctuations could be interrelated with the ordering of the interstitial voids, as proposed by Elliott. Christie et al. also proposed a model of disordered crystalline lattices that could reproduce the FSDP[29]. Similarly, the FSDPs

Correspondence: Akihiko Hirata (ahirata@aoni.waseda.jp) or
Motoki Shiga (motoki.shiga.b4@tohoku.ac.jp) or
Shinji Kohara (KOHARA.Shinji@nims.go.jp)
[1]Department of Materials Science, Waseda University, Tokyo 169-8555, Japan
[2]Kagami Memorial Research Institute for Materials Science and Technology, Waseda University, Tokyo 169-0051, Japan
Full list of author information is available at the end of the article

observed at $Q = 1$ to $2\,\text{Å}^{-1}$ correspond to the periodic fluctuations of 3–6 Å according to the relationship of $D = 2\pi/Q$, where D represents the spacing between the periodic fluctuations[19]. Moreover, the scale of the FSDP in real space exceeds that of the interatomic distances. Thus, the concept of quasilattice planes is quite helpful in understanding the FSDP with local anisotropy in the context of the IRO structures.

We recently utilized the angstrom-beam electron diffraction (ABED) technique to observe electron diffraction patterns from local atomic arrangements of glass structures[30–35]. As the beam size decreased to approximately 1 nm, the diffraction intensity changed from isotropic to anisotropic. In addition, the correspondence between the anisotropic diffraction intensity and the local atomic arrangement could be studied using the virtual ABED technique[35]. Thus, these techniques represent some of the most suitable tools for determining the anisotropic intensity of FSDP and revealing the relationship between the FSDP and the periodic density fluctuations in real space. In this study, we employ both ABED experiments and virtual ABED simulations to explore the origin of the FSDP in SiO_2 glass, a representative covalent glass. In particular, we use an energy filter and a cold field-emission electron gun to resolve the anisotropic FSDPs at low scattering angles ($Q = 0.9$ to $1.5\,\text{Å}^{-1}$).

Results

Angstrom-beam electron diffraction measurements

To obtain the anisotropic diffraction intensity of the local regions of SiO_2 glass, we performed an ABED experiment using a scanning transmission electron microscope (STEM), as shown in Fig. 1a. A focused electron probe was used to illuminate and scan the thin SiO_2 glass sample. Subsequently, the diffraction patterns for each local region were recorded by a CCD camera at the bottom. The full width at half maximum and convergence angle of the electron probe were 0.9 nm and 1.2 mrad, respectively. The diffraction patterns were obtained using elastic scattering through an energy filter device. A comparison between the filtered and unfiltered diffraction patterns is shown in Supplementary Fig. S1.

Figure 1b shows the pairs of diffraction spots observed at low scattering vectors ranging from $Q = 0.9$ to $1.5\,\text{Å}^{-1}$. The diffraction spot at $Q = 1.5\,\text{Å}^{-1}$ corresponded to the FSDP of the SiO_2 glass. All diffraction patterns were collected from different local regions of the sample. As shown in the figure, diffraction spots could be observed at the top of the FSDP ($Q = 1.5\,\text{Å}^{-1}$) and at the lower scattering vector of $Q \sim 0.9\,\text{Å}^{-1}$. The positions of the peaks are indicated by the structure factors $S(Q)$ of the high-energy X-ray and neutron diffraction, as shown in Fig. 1c. Because the slope of the $S(Q)$ curves changes significantly
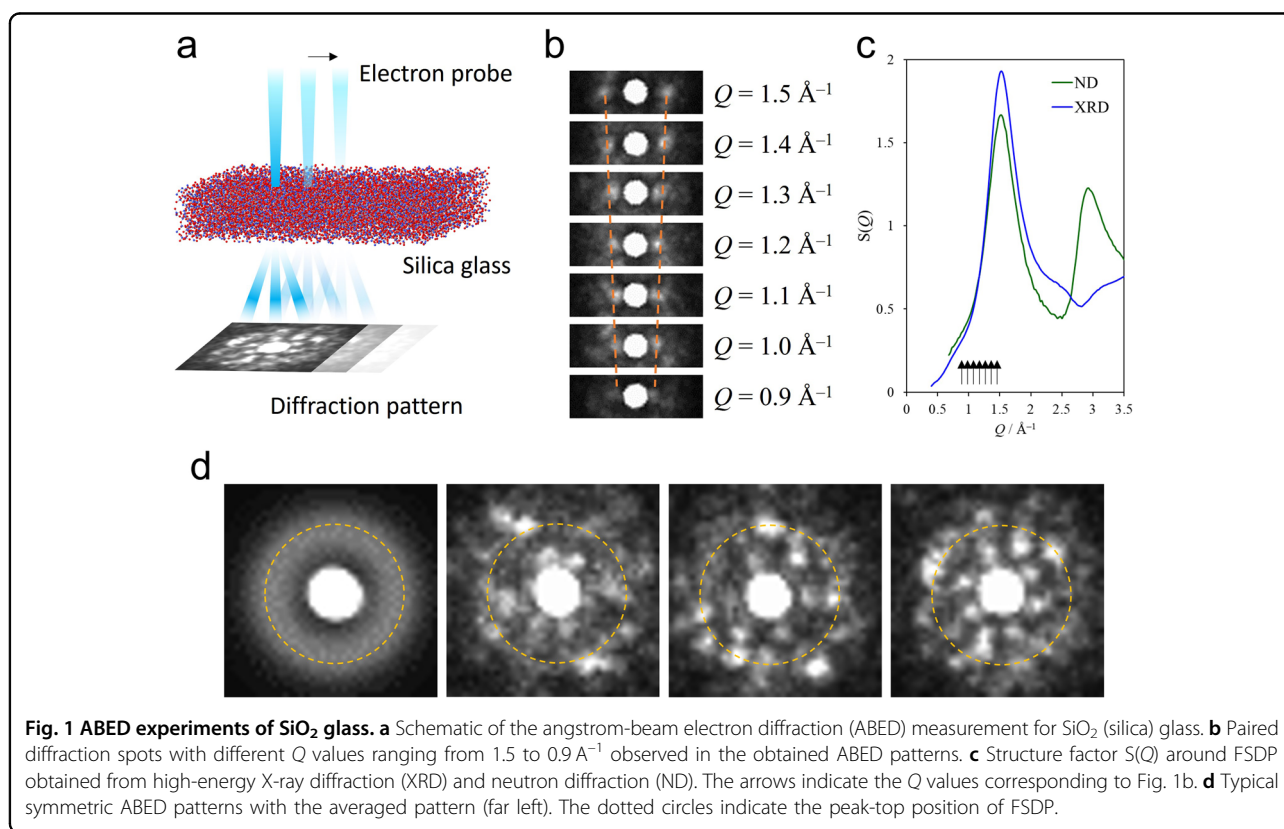
Fig. 1 ABED experiments of SiO₂ glass. a Schematic of the angstrom-beam electron diffraction (ABED) measurement for SiO₂ (silica) glass. **b** Paired diffraction spots with different Q values ranging from 1.5 to 0.9 Å⁻¹ observed in the obtained ABED patterns. **c** Structure factor $S(Q)$ around FSDP obtained from high-energy X-ray diffraction (XRD) and neutron diffraction (ND). The arrows indicate the Q values corresponding to Fig. 1b. **d** Typical symmetric ABED patterns with the averaged pattern (far left). The dotted circles indicate the peak-top position of FSDP.

around $Q = 1.2\,\text{Å}^{-1}$, we refer to the region below $Q = 1.2\,\text{Å}^{-1}$ as the shoulder of the FSDP. The shoulder was significantly reduced in the case of densified SiO_2 glass[36]. In addition, the ABED diffraction spots were also observed at the shoulder, as shown in Fig. 1b.

The typical symmetric two-dimensional experimental diffraction patterns were similar to the zone-axis patterns in crystals, as shown in Fig. 1d, with the averaged pattern on the far left (*also see* Supplementary Fig. S2). The averaged pattern consisted of the so-called halo rings, corresponding to the structure factor $S(Q)$ in Fig. 1c. In the three diffraction patterns on the right, we could observe the symmetric patterns formed by the spots with lower Q values than the top of the FSDP (dotted circles). By analogy with crystals, these two-dimensional patterns contained abundant structural information.

Extraction of the local atomic configurations by virtual angstrom-beam electron diffraction analysis

The simulation of the ABED experiment was conducted using a computer by following a similar process that included beam scanning[35]. We prepared a large-scale structural model of SiO_2 glass with dimensions of $10 \times 10 \times 10\,\text{nm}^3$ by a combined method of molecular dynamics and reverse Monte Carlo simulations. The details of the modeling procedure are described in a previous paper[36]. The obtained model was independently

created from ABED and could reproduce the high-energy X-ray and neutron diffraction experiments that provided the isotropic intensities, including FSDPs, as shown in Fig. 2a.

Our interest is whether the model based on isotropic intensities produces symmetric diffraction patterns with anisotropic intensities, as observed in the ABED experiment. To address the above statement, we conducted a virtual ABED analysis[35] for the model. While the model was based on isotropic intensities, it was constructed with constraints, such as coordination numbers and bond angle distributions, to ensure physical reasonableness, especially for the short-range structures. The 10-nm-thick model was sliced into 2-nm-thick models and then virtually scanned by an electron beam with a 0.2-nm step (Fig. 2b). Note that the edge portions of the crushed glassy samples were estimated to be ~2–3 nm[34]. The electron diffraction patterns calculated from each local region were stored in a database together with the coordinates of the electron beam positions. An example of a series of diffraction patterns is shown in Fig. 2c. Note that the array of the diffraction patterns (6×6) in Fig. 2c coincides with the electron beam positions (6×6) in real space, as shown in Fig. 2b. By carefully inspecting the diffraction patterns, symmetric patterns can be observed and are marked in red. We retrieved the clearest pattern marked in red from the dataset containing several similar patterns.
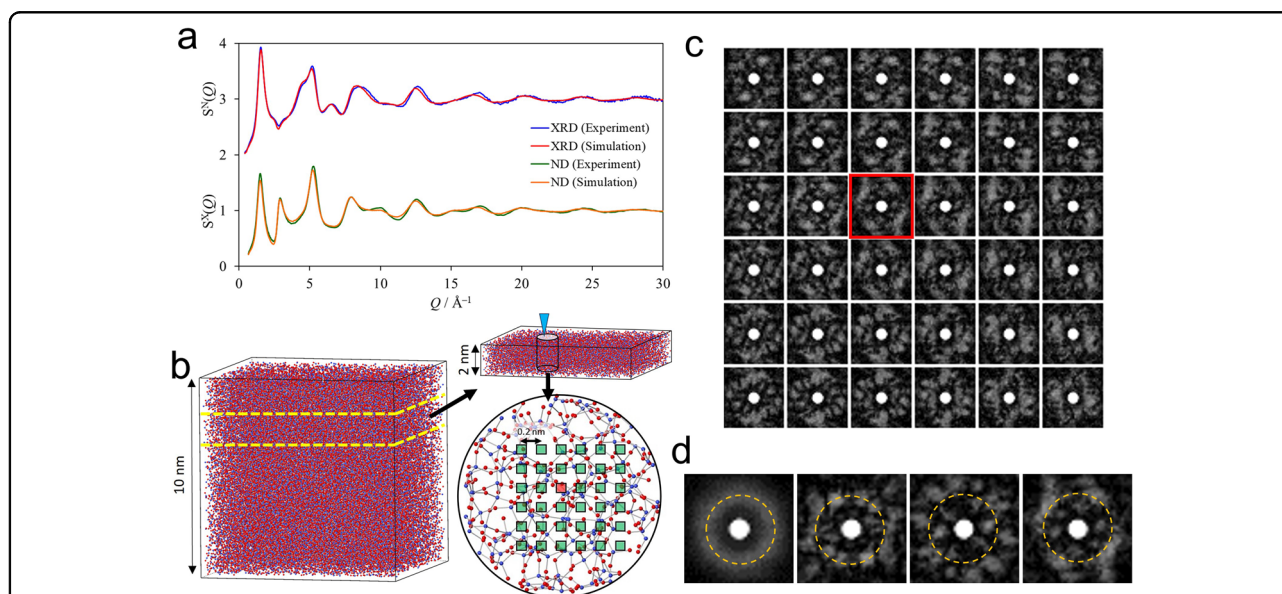
Fig. 2 ABED simulation for the structural model of SiO$_2$ glass. a X-ray and neutron structure factors ($S^X(Q)$ and $S^N(Q)$) obtained from the structural model of SiO$_2$. Both experimentally obtained structure factors ($S^X(Q)$ and $S^N(Q)$) are also shown. **b** Structural model of SiO$_2$ glass obtained by combining molecular dynamics (MD) and reverse Monte Carlo (RMC) simulations. The obtained model is sliced into thin models of 2 nm thickness for virtual ABED analysis. The electron probe is virtually irradiated on the thin model in 0.2 nm steps. The top view of the selected cylindrical region in the thin model is also shown with 6×6 beam positions. **c** Example of a partial dataset of ABED patterns obtained by virtual electron probe scanning of the 6×6 beam positions shown in (**b**). **d** Typical simulated ABED patterns found in the dataset with the averaged pattern (far left). The dotted rings indicate the peak position of FSDP. Note that the far-right pattern is identical to the marked pattern in (**c**).

Fig. 3 Atomic density fluctuations for the extracted structural model. a Projection of the extracted cylindrical structural model. The diameter and height of the cylinder are both 2 nm. The red and blue circles represent O and Si atoms, respectively. The simulated ABED pattern obtained from the central part of the model is also shown in the inset. The electron incidence of the ABED pattern is parallel to the projection direction. **b** Side views of the atomic configurations obtained from region I and region II of (**a**). Note that the three atoms marked by a dotted oval circle exist slightly outside the column. **c, d** Inverse fast Fourier transform (FFT) images constructed using the marked spots of the corresponding FFT patterns shown in the insets. The FFT pattern is obtained from the projection image of (**a**). The atomic configuration of (**a**) is superimposed on the inverse FFT images.
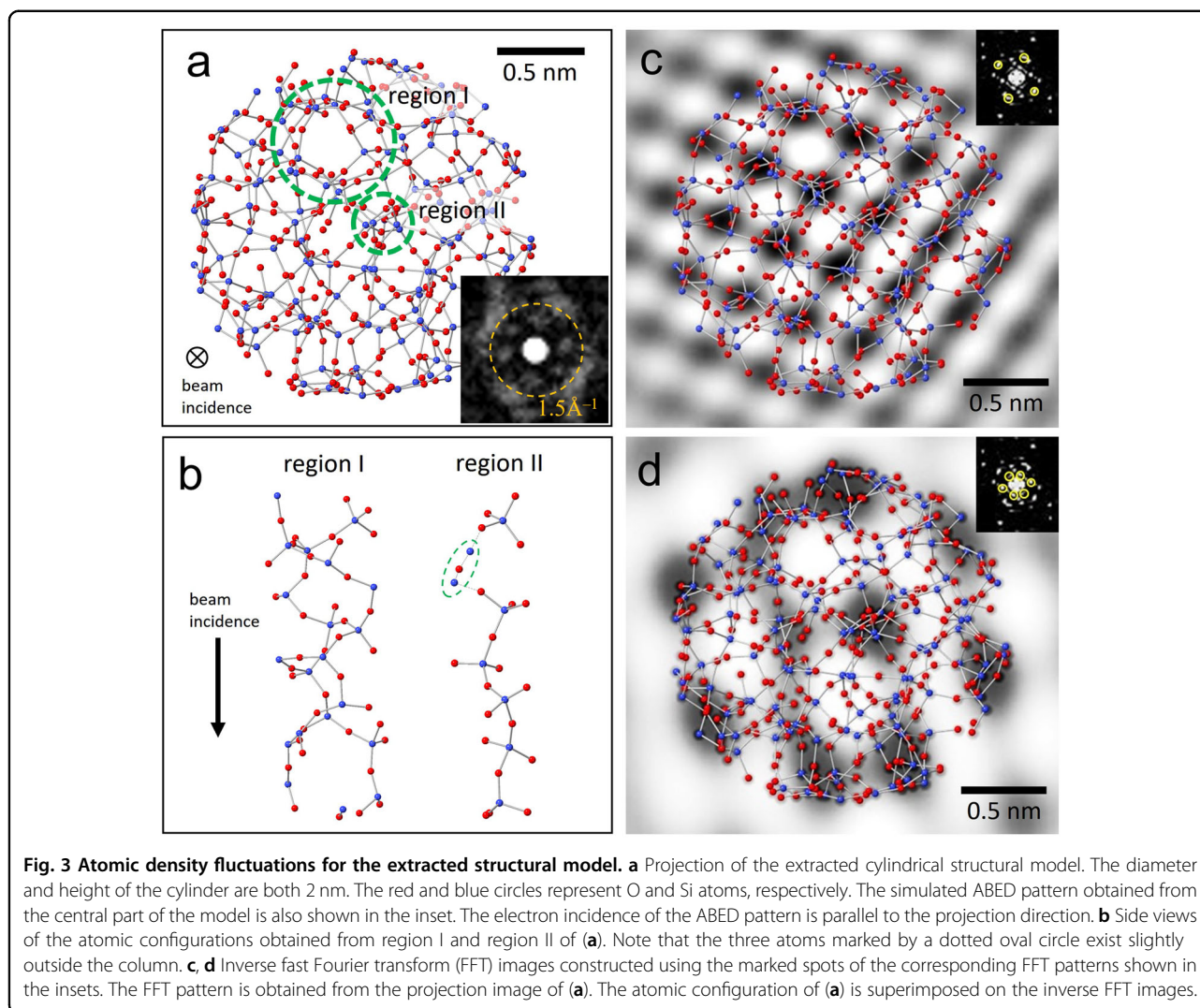
Figure 2d shows three examples of symmetric diffraction patterns, including the pattern shown in Fig. 2c, together with the averaged pattern on the far left. The dotted circles indicate the top position of the FSDP. The patterns consisting of six spots within FSDP correspond to the shoulder in the $S(Q)$ profile of Fig. 1c and can be clearly observed. Thus, the structural model based on the isotropic structure factor $S(Q)$ contains the local atomic arrangements that produce the symmetric diffraction patterns with anisotropic intensities, as observed experimentally. Here, we focus on the symmetric pattern consisting of six spots shown on the far-right side of Fig. 2d; this pattern has similar features to the experimental pattern shown on the far-right side of Fig. 1d.

To understand the structural origin of the symmetric diffraction patterns of FSDP and its shoulder, we extracted the local atomic configurations that generated these patterns from the original structural model of Fig. 2b. Figure 3a shows the extracted atomic configuration of

SiO_2 corresponding to the symmetric diffraction pattern of the inset; this is identical to the pattern marked in red in Fig. 2c and the far-right pattern of Fig. 2d. In the calculation of the diffraction pattern, the electron probe was irradiated at the center of the structural model. The four spots with strong intensities are observed near the FSDP, and six spots can be observed inside. From this incidence direction, the atomic density fluctuations in the structural model can be observed as sparse regions (e.g., region I) and dense regions (e.g., region II).

Figure 3b shows the side views of the atomic arrangements of region I and region II corresponding to the sparse and dense regions of the atomic density, respectively. In region I, a tubular atomic configuration of at least 2 nm in length is formed where a rod-shaped void is surrounded by atoms (*see* Supplementary Fig. S3). Conversely, a chain-like columnar atomic configuration is found in region II, where the local atomic density is relatively high. Similar features can be found in another

region of the same model, as shown in Supplementary Fig. S4. Thus, the virtual ABED technique reveals that the atomic density fluctuation with local two-dimensionality is formed in the structural model created based on the isotropic structure factors.

As mentioned in the introduction, the local periodicity in the atomic density characterized by $2\pi/Q$ could be related to the FSDPs in reciprocal space. We employed fast Fourier transform (FFT) and inverse FFT techniques (*see* Supplementary Fig. S5) to understand the correspondence between the periodic fluctuations in atomic density[19] and FSDPs. The FFT pattern obtained from the projected image of the atomic configuration in the insets of Fig. 3c, d is consistent with the calculated diffraction pattern shown in the inset of Fig. 3a. Figure 3c shows the inverse FFT image constructed from the four spots observed at the FSDP position in the corresponding FFT pattern, together with the projected atomic configuration. The dense regions of the structural model nearly coincide with the dark regions of the inverse FFT image. Similarly, the inverse FFT image generated by the six spots inside the FSDP is shown in Fig. 3d. An atomic density fluctuation with a longer periodicity (~ 0.52–0.57 nm) than that in Fig. 3c (~ 0.41 nm) is also observed in the same structural model.

To confirm the correlation between the contrast variations in the inverse FFT images and the atomic density fluctuations, we performed kernel density estimation with a Gaussian kernel[37] for the local structural model shown in Fig. 3a. This method enables the determination of the atomic density distributions by constructing smooth symmetric functions for each projected atomic position. Supplementary Fig. S6a shows the density map for the model of Fig. 3a obtained by the kernel density estimation. The two different inverse FFT images shown in Fig. 3c, d are superimposed on this map, as shown in Supplementary Figs. S6b and S6c, respectively. The map obtained by kernel density estimation is basically consistent with the contrast variations in the inverse FFT images.
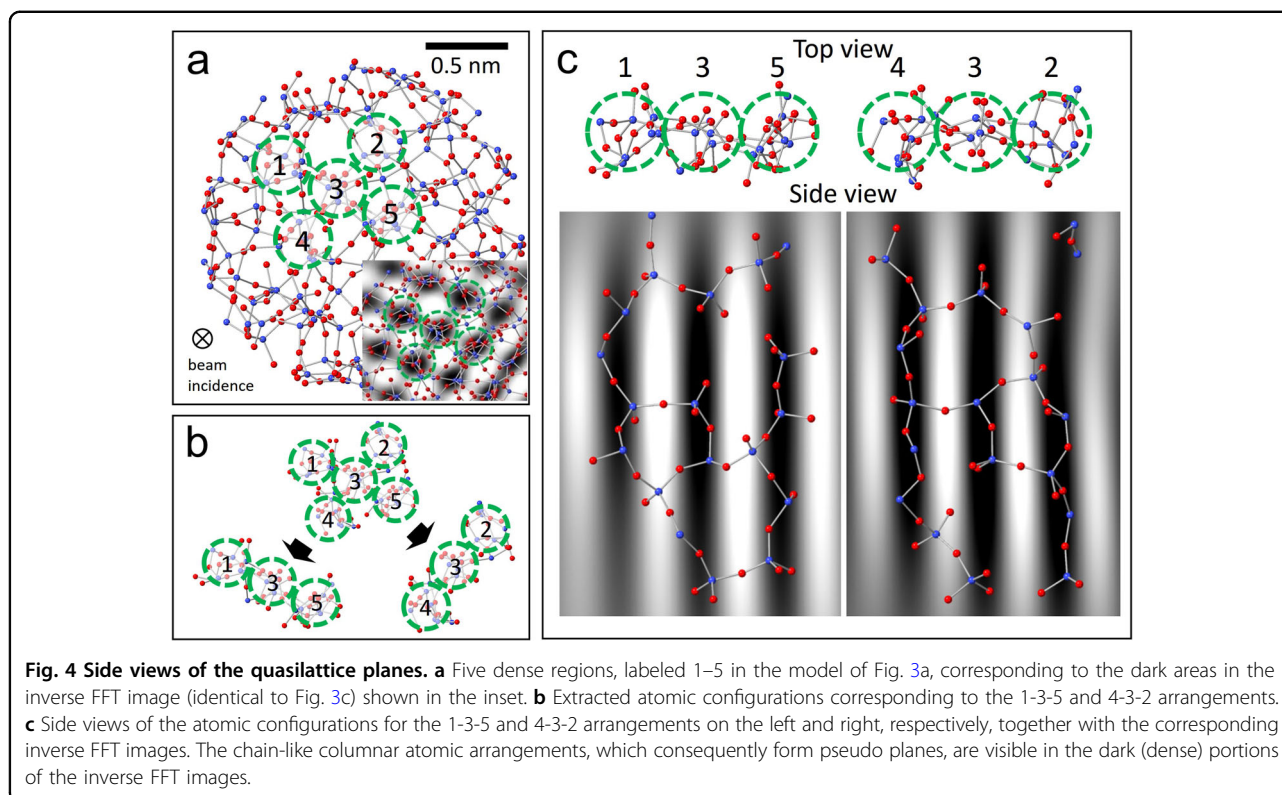
Discussion

In the present study, we experimentally obtained characteristic two-dimensional diffraction (ABED) patterns related to FSDP from local regions of SiO_2 glass and extracted the corresponding atomic arrangements. The periodic fluctuations in the atomic density could be interpreted as alternating arrangements of chain-like columnar atomic configurations and interstitial tubular voids, as shown in Fig. 3b. Note that the interstitial tubular voids are longitudinally limited to a size of approximately 2 nm (*see* Supplementary Fig. S7). These columnar objects do not necessarily correspond to two-dimensional structures because the atomic density fluctuation is technically challenging to confirm over the other orientations.

Next, we discuss how the arrangements of columnar objects relate to the concept of quasilattice planes proposed in a previous study[19]. As shown in Fig. 4a, we focus on the five chain-like columnar atomic configurations corresponding to the dense regions. The two types of arrangements consisting of the 1-3-5 and 4-3-2 columns are extracted from the model, as shown in Fig. 4b. Figure 4c shows the side views of the 1-3-5 and 4-3-2 arrangements and their corresponding inverse FFT images. From these orientations, pseudo-two-dimensional atomic arrangements, which could be called quasilattice planes, can be observed with atomic density fluctuations. The chain-like columnar atomic configurations are formed in the dense regions (dark regions in the inverse FFT images), and each is connected by bridge atoms located in the sparse regions (bright regions). Notably, the arrangements of the 1-3-5 columns and 4-3-2 columns intersect, similar to the observations in crystals. The description mentioned above is fairly consistent with the concept of quasilattice planes, but we believe that our present results provide a more specific description in terms of their similarity to crystals.

Here, the quasi-crystalline models proposed by Phillips are discussed[38,39]. In this model, the structure of silica glass consists of an aggregate of β-cristobalite paracrystals with a size of 66 Å. The boundaries between the paracrystals are assumed to be filled with a structure similar to the grain boundaries of crystalline materials. However, a subsequent study[40] noted that this model was not consistent with the neutron diffraction data. According to our study, even when the crystal size is less than 10 Å, the simulated structure factor does not agree with the simulated structure factor. Our present observation also does not support the quasi-crystalline models because the experimental ABED patterns are reasonably consistent with those calculated from the non-crystalline model that is based on the X-ray and neutron diffraction data. The presence of 5- and 7-membered rings, which are not found in crystals[41], is also indicative of the non-crystalline features of our model (Supplementary Fig. S8). Notably, the term quasilattice planes is used for non-crystalline structures, and the presence of diffraction spots in the ABED patterns does not necessarily indicate the presence of crystal structures.

Furthermore, diffraction spots are distinct from the Bragg reflections of crystal structures and can be generated from non-crystalline structures. For example, when considering the diffraction intensity of a single molecule, a distinct intensity distribution is generated in a three-dimensional reciprocal space. This intensity distribution is caused by the presence of a correlation term in the diffraction intensity equation[34]. Similarly, the diffraction intensity from the local atomic arrangements of the glasses also has a three-dimensional intensity distribution.

Fig. 4 Side views of the quasilattice planes. a Five dense regions, labeled 1–5 in the model of Fig. 3a, corresponding to the dark areas in the inverse FFT image (identical to Fig. 3c) shown in the inset. **b** Extracted atomic configurations corresponding to the 1-3-5 and 4-3-2 arrangements. **c** Side views of the atomic configurations for the 1-3-5 and 4-3-2 arrangements on the left and right, respectively, together with the corresponding inverse FFT images. The chain-like columnar atomic arrangements, which consequently form pseudo planes, are visible in the dark (dense) portions of the inverse FFT images.
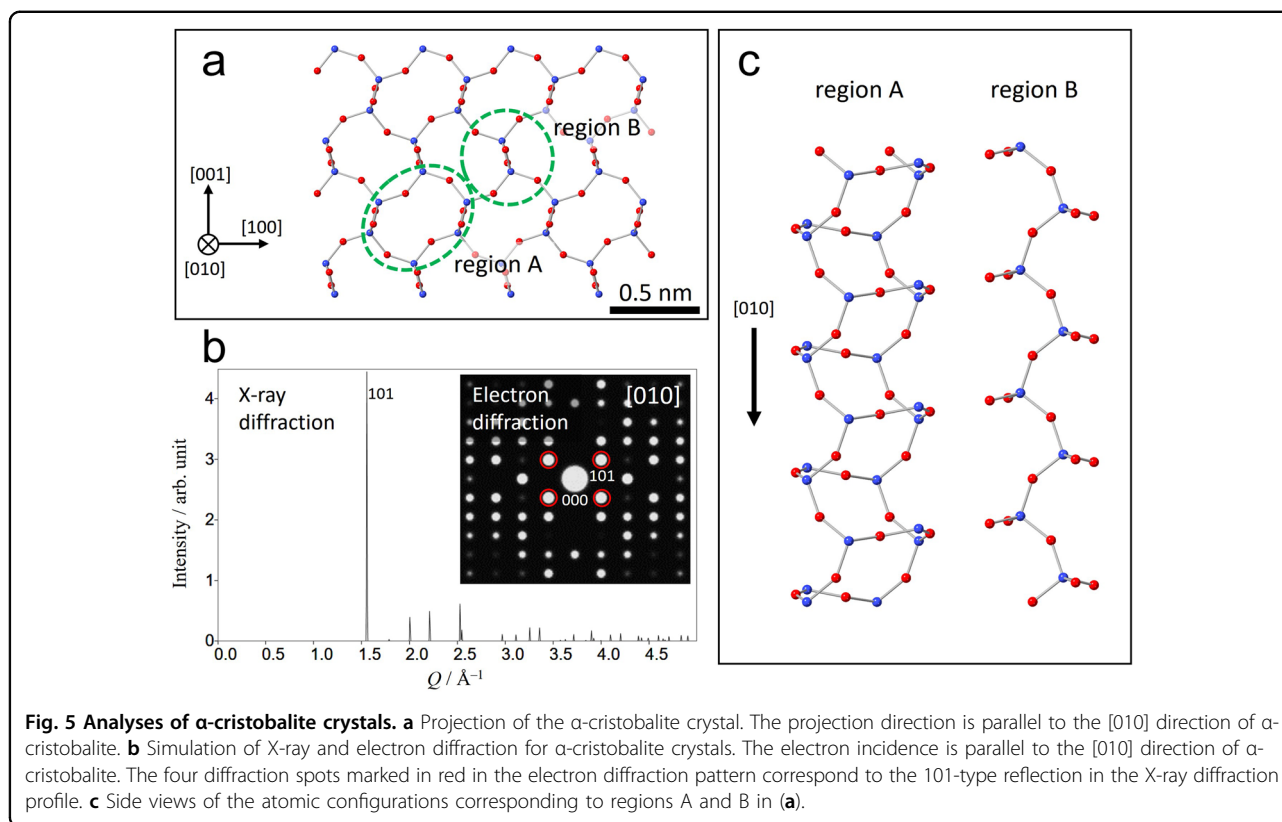
As the size of the local structures increases (*see* Supplementary Fig. S9), the diffraction pattern gradually becomes isotropic halo rings; these results are basically consistent with the X-ray and neutron diffraction profiles. Specifically, the diffraction spots observed in this study can be viewed as the building blocks of the halo rings due to their glass structures (*also see* Supplementary Fig. S10).

Next, we consider examples of the SiO_2 crystals for comparison with the glass structures. In the case of α-cristobalite with a density of 2.33 g cm^{-3}, the sparse and dense portions denoted by regions A and B in the projection of Fig. 5a are similar to the glass structures of regions I and II in Fig. 3 and correspond to the columnar configurations along the projection direction, as shown in Fig. 5c. Alternating arrangements of the columnar atomic configurations and interstitial tubular voids can also be observed in the figure. Additionally, the four 101-type spots ($Q = 1.56\,\text{Å}^{-1}$) corresponding to the FSDP in the glass in the simulated electron diffraction pattern for α-cristobalite are closely related to the alternating arrangements in real space, as shown in Fig. 5b. Similar features are also found in the α-quartz crystal with a density of 2.66 g cm^{-3}, as shown in Supplementary Fig. S11. However, in this case, the 011-type reflections potentially correspond to the FSDP in the glass because the intensity of 011 is much stronger than the intensity of 100, and the density of α-quartz is much greater than that of glass (2.21 g cm^{-3}). In addition, the 100-type reflections, which

form the sixfold electron diffraction pattern, more likely correspond to the shoulder of the FSDP. A similar pattern consisting of six spots is observed in the glass model, as shown in Fig. 3a. Thus, the local structures of glasses are not exactly the same as those of crystals but have somewhat similar characteristics. Notably, the anisotropic nature is only local in glassy structures, as opposed to the macroscopic anisotropy in crystals.

To confirm the relationship between the atomic density fluctuations and inverse FFT images of the crystals, FFT analyses on the crystals were performed similarly to those performed on the above glass samples. Supplementary Fig. S12 shows inverse FFT images for α-cristobalite, α-quartz, and coesite (*see also* Supplementary Fig. S13) crystals superimposed on each atomic configuration, along with their corresponding FFT patterns. Similar to glass structures, the dark regions coincided with a high atomic density, while the bright regions coincided with a low atomic density. From these crystal examples, the contrast of light and dark regions in the inverse FFT images corresponded to the sparse and dense regions with respect to the atomic density. Notably, the bright regions in the coesite corresponded to the arrangements of the smaller 4-membered rings compared to those in the other crystals.

The structural characteristics of network glasses have often been investigated through ring statistics analysis[12]. The correlation between the sizes of the rings and the

Fig. 5 Analyses of α-cristobalite crystals. a Projection of the α-cristobalite crystal. The projection direction is parallel to the [010] direction of α-cristobalite. **b** Simulation of X-ray and electron diffraction for α-cristobalite crystals. The electron incidence is parallel to the [010] direction of α-cristobalite. The four diffraction spots marked in red in the electron diffraction pattern correspond to the 101-type reflection in the X-ray diffraction profile. **c** Side views of the atomic configurations corresponding to regions A and B in (**a**).

atomic density fluctuations from our study are investigated. As shown in Supplementary Figs. S8b and S8e, we calculated Guttman-type ring distributions for the thick atomic columns shown in Supplementary Fig. S14a and S14c, respectively; moreover, we calculated the ring-distributions for both the local structures (Figs. S8a and S8b) and the total structure (Fig. S8f). In these atomic columns, the proportions of 7-membered rings, whose sizes are relatively large, are quite high compared to those of the total structure. In addition, the spatial distributions of the ring centers together with the inverse FFT images of Fig. 3c, d are shown in Supplementary Fig. S15. Supplementary Figs. S15a and S15b show the distributions of the central points for the rings with five members or fewer and the rings with six members or more, respectively; these distributions are superimposed in Fig. 3c. The distributions with five members or fewer and six members or more are superimposed on Fig. 3d and are also shown in Supplementary Figs. S15c and S15d. According to Supplementary Figs. S15a and S15b, the distributions of the points are relatively uniform, and numerous points are located in the bright regions in the inverse FFT image of Fig. 3c. Considering the directions of the normal vectors in Supplementary Fig. S16, the rings could function as bridges connecting the denser regions, as depicted in Fig. 4c. On the other hand, as shown in Supplementary Fig. S15d, the distribution of rings with six members or

more correlates well with the inverse FFT image of Fig. 3d, which has longer periods because most of the points are near the darker regions. The directions of the normal vectors shown in Supplementary Fig. S16 indicate that the rings around the darker regions presumably form the outer walls of the larger tubular voids (*also see* Fig. S14c). Additionally, some points with normal vectors close to the direction of incidence can be found in the center of the bright regions; thus, the ring itself surrounds the tubular column, as shown in Fig. S14a. Therefore, the larger rings are related to the longer periods originating from the shoulder of the FSDP, similar to the case of the crystals mentioned above.

Discussing the spatial extent of the IRO is also important. Supplementary Fig. S17 shows two sequential series of experimental ABED patterns captured in 0.25 nm steps. Identical diffraction spots indicated by the red arrows are located at the peak top of FSDP and are consistently observed over 3 steps in both cases. Considering the beam size of 0.9 nm, the spatial extent of the order is roughly estimated to be from 0.9 to 1.4 nm. Similarly, from the simulation side, the higher contrast region of the inverse FFT image is also extended, as shown in Supplementary Fig. S18. The extension estimated by ABED is consistent with that estimated by X-ray diffraction (approximately 1 nm)[36]. However, different from crystals, evident interfaces between IRO do

not exist; therefore, the extent of the IRO is not easily determined experimentally.

According to previous work reported by Salmon et al. [20], AX_2-type network glasses possessed topological and chemical ordering on two different length scales according to neutron diffraction measurements with an isotopic substitution technique. One scale was an intermediate range order manifested by an FSDP, and the other scale was manifested by the principal peak at a higher scattering angle than the FSDP. Notably, the latter ordering was an extended-range order with a periodicity of 3.14 Å, where the oscillations in the pair distribution function were calculated to be 6.2 nm. In contrast, in the present study, the arrangement of the columnar objects generates hierarchical structures with different length scales corresponding to the FSDP and its shoulder at the low Q side (*see* Figs. 3c, d). We show that the diffraction spots around the FSDP with different scattering angles originate from identical local atomic configurations, producing the wide distribution of the FSDP, including the shoulder, found in the X-ray and neutron structure factors. Specifically, the FSDP is not a single peak but a composite of multiple peaks. The local structures of glass do not exactly correspond to the crystals, as mentioned above. However, they have partially similar features with some periodic fluctuations in the atomic density. For example, the structure corresponding to the shoulder can have similar features to α-quartz despite a shift in the Q position of α-quartz caused by density differences between α-quartz and α-cristobalite/glass. The characteristic spatial fluctuations or inhomogeneities, which cannot be described by the average values, are needed to control the properties and performance of disordered materials beyond the average[42]. In addition, when high pressure is applied, the longer period in the densified SiO_2 glass presumably disappears due to the decrease in the shoulder, as well as the prominent peak shift[36]. Considering the stability of ordinary SiO_2 glass and its densification mechanism, future studies should focus on the longer periodic fluctuations associated with the shoulder.

Methods

Angstrom-beam electron diffraction (ABED) measurements

ABED experiments were performed with an aberration-corrected scanning transmission electron microscope (Titan cubed, Thermo Fisher Scientific, operated at 300 kV) equipped with a cold field-emission electron gun. All ABED patterns were acquired by scanning the focused electron probe with an exposure time of 0.01 s and a scan step of 0.25 nm. The convergence angle of the probe and the probe size were 1.2 mrad and 0.9 nm, respectively. Inelastic electron scattering was eliminated from the ABED patterns using an electron energy loss spectroscope. The samples for ABED observation were prepared by crushing a commercial SiO_2 glass sample (T-4040, Covalent Materials Corp.).

Structure modeling

The atomic configuration of the SiO_2 glass was obtained by a combination of molecular dynamics (MD) and reverse Monte Carlo (RMC) simulations. First, a random atomic configuration containing 22,052 Si atoms and 44,104 O atoms was prepared in a simulation box with dimensions of $10 \times 10 \times 10$ nm^3 and a density of 2.21 g cm^{-3}. The initial configuration was held at 4000 K for 1.0×10^5 steps to equilibrate to the liquid state, followed by cooling to 300 K for 5.0×10^6 steps and relaxation at 300 K for 1.0×10^5 steps. The time step was set to 1 fs. The MD simulation was performed by the LAMMPS code[43] under the NVT ensemble, where the number of atoms, the volume, and the temperature were kept constant, using the Verlet algorithm. Interatomic pair potentials with short-range Born−Mayer repulsive and long-range Coulomb terms were employed. The configuration obtained by MD was further modified to fit the experimental X-ray and neutron structure factors by the RMC simulation using the RMC + + code[44–46]. The RMC simulation was performed by considering the constraints on the coordination numbers, O−Si−O bond angles, and partial pair-distribution functions within the first coordination shell. These constraints were incorporated to maintain the physically reasonable structures generated by the MD simulation. The details of the diffraction experiments and simulations are described in a previous paper[36].

Virtual angstrom-beam electron diffraction analysis

Electron diffraction patterns for the 1681 (41×41) positions of the structural model obtained by a combination of MD and RMC were calculated sequentially at 0.2 nm intervals using a multislice method[47]. The accelerating voltage, defocus value, and third-order spherical aberration coefficient were 300 kV, 0 nm, and 0.005 mm, respectively. The convergence semi-angle of the electron probe was set to 1.2 mrad. The symmetric diffraction patterns were selected from the obtained dataset containing 1681 patterns. Subsequently, we extracted the atomic configurations around the position where the electron probe was virtually irradiated. The FFT of the projection images of the extracted structural models and the inverse FFT were performed using a Gatan DigitalMicrograph 3.5.

Author details
[1]Department of Materials Science, Waseda University, Tokyo 169-8555, Japan. [2]Kagami Memorial Research Institute for Materials Science and Technology, Waseda University, Tokyo 169-0051, Japan. [3]WPI Advanced Institute for Materials Research, Tohoku University, Sendai 980-8577, Japan. [4]Mathematics for Advanced Materials-OIL, National Institute of Advanced Industrial Science and Technology, Sendai 980-8577, Japan. [5]Center for Basic Research on Materials, National Institute for Materials Science, Tsukuba 305-0047, Japan. [6]Faculty of Science and Technology, Tokyo University of Science, 2641 Yamazaki, Noda, Chiba, Japan. [7]Unprecedented-scale Data Analytics Center, Tohoku University, 468-1 Aoba, Aramaki-Aza, Aoba-ku, Sendai 980-8578, Japan. [8]Graduate School of Information Science, Tohoku University, 6-3-09 Aoba, Aramaki-aza Aoba-ku, Sendai 980-8579, Japan. [9]RIKEN Center for Advanced Intelligence Project, 1-4-1 Nihonbashi, Chuo-ku, Tokyo 103-0027, Japan. [10]Institute for Integrated Radiation and Nuclear Science, Kyoto University, 2-1010 Asashiro-nishi, Kumatori-cho, Sennan-gun, Osaka, Japan

Author contributions
A.H. and S.K. conceived this study. A.H., S.S. and K.K. performed the ABED experiments and analyses. A.H. and M.S. contributed to the virtual ABED analyses. M.S., Y.O. and S.K. performed the structural modeling. M.S. performed the ring distribution analyses and kernel density estimation. A.H. wrote the manuscript, and all the authors discussed the results and commented on the manuscript.

Conflict of interest
The authors declare no competing interests.

References
1. Elliott, S. R. *Physics of Amorphous Materials*. 2nd ed (Longman, London, UK, 1990).
2. Zallen, R. *The Physics of Amorphous Solids*. Wiley: New York, NY, USA, 1983.
3. Elliott, S. R. Medium-range structural order in covalent amorphous solids. *Nature* **354**, 445–452 (1991).
4. Sokolov, A. P., Kisliuk, A., Soltwisch, M. & Quitmann, D. Medium-range order in glasses: Comparison of Raman and diffraction measurements. *Phys. Rev. Lett.* **69**, 1540–1543 (1992).
5. Kohara, S. & Salmon, P. S. Recent advances in identifying the structure of liquid and glassy oxide and chalcogenide materials under extreme conditions: A joint approach using diffraction and atomistic simulation. *Adv. Phys. X* **1**, 640–660 (2016).
6. Huang, P. Y. et al. Direct Imaging of a Two-Dimensional Silica Glass on Graphene. *Nano Lett.* **12**, 1081–1086 (2012).
7. Evans, D. L. & King, S. V. Random network model of vitreous silica. *Nature* **212**, 1353–1354 (1966).
8. King, S. V. Ring Configurations in a random network model of vitreous silica. *Nature* **213**, 1112–1113 (1967).
9. Sharma, S. K., Mammone, J. F. & Nicol, M. F. Raman investigation of ring configurations in vitreous silica. *Nature* **292**, 140–141 (1981).
10. Wright, A. C. Neutron scattering from vitreous silica. V. The structure of vitreous silica: What have we learned from 60 years of diffraction studies?. *J. Non-Cryst. Solids* **179**, 84–115 (1994).
11. Roux, S. L. & Jund, P. Ring statistics analysis of topological networks: New approach and application to amorphous GeS_2 and SiO_2 systems. *Comput. Mater. Sci.* **49**, 70–83 (2010).
12. Shi, Y. et al. Ring size distribution in silicate glasses revealed by neutron scattering first sharp diffraction peak analysis. *J. Non-Cryst. Solids* **516**, 71–81 (2019).
13. Kohara, S. et al. Relationship between diffraction peak, network topology, and amorphous-forming ability in silicon and silica. *Sci. Rep.* **11**, 1–11 (2021).
14. Price, D. L., Moss, S. C., Reijers, R., Saboungi, M.-L. & Susman, S. Intermediate-range order in glasses and liquids. *J. Phys. C Solid State Phys.* **21**, L1069–L1072 (1988).
15. Elliott, S. R. Origin of the first sharp diffraction peak in the structure factor of covalent glasses. *Phys. Rev. Lett.* **67**, 711–714 (1991).
16. Elliott, S. R. Origin of the first sharp diffraction peak in the structure factor of covalent glasses and liquids. *J. Phys. Condens. Matter* **4**, 7661–7678 (1992).
17. Chechetkina, E. A. The first sharp diffraction peak in glasses and in other amorphous substances. *J. Phys. Condens. Matter* **5**, L527 (1993).
18. Salmon, P. S. Real space manifestation of the first sharp diffraction peak in the structure factor of liquid and glassy materials. *Proc. R. Soc. A Math. Phys. Eng. Sci.* **445**, 351–365 (1994).
19. Gaskell, P. H. & Wallis, D. J. Medium-range order in Silica, the canonical network glass. *Phys. Rev. Lett.* **76**, 66–69 (1996).
20. Salmon, P. S., Martin, R. A., Mason, P. E. & Cuello, G. J. Topological versus chemical ordering in network glasses at intermediate and extended length scales. *Nature* **435**, 75–78 (2005).
21. Crupi, C., Carini, G., González, M. & D'Angelo, G. Origin of the first sharp diffraction peak in glasses. *Phys. Rev. B* **92**, 134206 (2015).
22. Uchino, T., Harrop, J. D., Taraskin, S. N. & Elliott, S. R. Real and reciprocal space structural correlations contributing to the first sharp diffraction peak in silica glass. *Phys. Rev. B* **71**, 014202 (2005).
23. Elliott, S. R. Extended-range order, interstitial voids and the first sharp diffraction peak of network glasses. *J. Non-Cryst. Solids* **182**, 40–48 (1995).
24. Gaskell, P. H. Medium-range structure in glasses and low-Q structure in neutron and X-ray scattering data. *J. Non. Cryst. Solids* **351**, 1003–1013 (2005).
25. Du, J. & Corrales, L. R. Compositional dependence of the first sharp diffraction peaks in alkali silicate glasses: A molecular dynamics study. *J. Non-Cryst. Solids* **352**, 3255–3269 (2006).
26. Chechetkina, E. A. Is there a relation between glass-forming ability and first sharp diffraction peak? *J. Phys. Condens. Matter* **7**, 3099–3114 (1995).
27. Zeidler, A. & Salmon, P. S. Pressure-driven transformation of the ordering in amorphous network-forming materials. *Phys. Rev. B* **93**, 214204 (2016).
28. Börjesson, L., Hassan, A. K., Swenson, J., Torell, L. M. & Fontana, A. Is there a correlation between the first sharp diffraction peak and the low frequency vibrational behavior of glasses? *Phys. Rev. Lett.* **70**, 1275–1278 (1993).
29. Christie, J. K., Taraskin, S. N. & Elliott, S. R. Structural characteristics of positionally disordered lattices: Relation to the first sharp diffraction peak in glasses. *Phys. Rev. B* **70**, 134207 (2004).
30. Hirata, A. et al. Direct observation of local atomic order in a metallic glass. *Nat. Mater.* **10**, 28–33 (2011).
31. Hirata, A. et al. Geometric frustration of icosahedron in metallic glasses. *Science* **341**, 376–379 (2013).
32. Hirata, A. et al. Atomic-scale disproportionation in amorphous silicon monoxide. *Nat. Commun.* **7**, 1–7 (2016).
33. Hirata, A., Ichitsubo, T., Guan, P. F., Fujita, T. & Chen, M. W. Distortion of local atomic structures in amorphous Ge-Sb-Te phase change materials. *Phys. Rev. Lett.* **120**, 205502 (2018).
34. Hirata, A. Local structure analysis of amorphous materials by angstrom-beam electron diffraction. *Microscopy* **70**, 171–177 (2021).
35. Hirata, A. Virtual angstrom-beam electron diffraction analysis for $Zr_{80}Pt_{20}$ metallic glasses. *Quantum Beam Sci.* **6**, 28 (2022).
36. Onodera, Y. et al. Structure and properties of densified silica glass: characterizing the order within disorder. *NPG Asia Mater.* **12**, 85 (2020).
37. Scott, D. W. Multivariate Density Estimation: Theory, Practice, and Visualization, John Wiley & Sons, New York (1992).
38. Phillips, J. C. Spectroscopic and Morphological Structure of Tetrahedral Oxide Glasses. *Solid State Phys.* **37**, 93–171 (1983).
39. Phillips, J. C. Microscopic origin of anomalously narrow Raman lines in network glasses. *J. Non-Cryst. Solids* **63**, 347–355 (1984).
40. Galeener, F. L. & Wright, A. C. The J. C. Phillips model for vitreous SiO_2: A critical appraisal. *Solid State Commun.* **57**, 677–682 (1986).

41. Shiga, M. et al. Ring-originated anisotropy of local structural ordering in amorphous and crystalline silicon dioxide. *Commun Mater* **4**, 91 (2023).

42. Kirchner, K. A. et al. Beyond the average: spatial and temporal fluctuations in oxide glass-forming systems. *Chem. Rev.* **123**, 1774–1840 (2022).

43. Thompson, A. P. et al. LAMMPS—A flexible simulation tool for particle-based materials modeling at the atomic, meso, and continuum scales. *Comput. Phys. Commun.* **271**, 108171 (2022).

44. McGreevy, R. L. & Pusztai, L. Reverse Monte Carlo simulation: A new technique for the determination of disordered structures. *Mol. Simul.* **1**, 359–367 (1988).

45. McGreevy, R. L. Reverse Monte Carlo modelling. *J. Phys. Condens. Matter.* **13**, R877 (2001).

46. Kohara S., Pusztai L. Atomistic Simulation of Glasses, Ed. by J. Du and A. N. Cormack, Wiley-American Ceramic Society, Hoboken pp. 60–88, 2022.

47. Kirkland, E. J. Advanced Computing in Electron Microscopy; Plenum: New York, NY, USA, 1998.